Silver(II) route to unconventional superconductivity

Xiaoqiang Liu,[1,*] Shishir K. Pandey,[1,*] and Ji Feng ⓘ[1,2,3,†]

[1]*International Center for Quantum Materials, School of Physics, Peking University, Beijing 100871, China*
[2]*Collaborative Innovation Center of Quantum Matter, Beijing 100871, China*
[3]*CAS Center for Excellence in Topological Quantum Computation, University of Chinese Academy of Sciences, Beijing 100190, China*

The highly unusual divalent silver in silver difluoride (AgF_2) features a nearly square lattice of Ag^{+2} bridged by fluorides. As a structural and electronic analog of cuprates, its superconducting properties are yet to be examined. Our first-principles electronic structure calculations reveal a striking resemblance between AgF_2 and the cuprates. Computed spin susceptibility shows a magnetic instability consistent with the experimentally observed antiferromagnetic transition. A linearized Eliashberg theory in the fluctuation-exchange approximation shows an unconventional singlet d-wave superconducting pairing for bulk AgF_2 at an optimal electron doping. The pairing is found to strengthen with decreasing interlayer coupling, highlighting the importance of the quasi-two-dimensional nature of the crystal structure. These findings place AgF_2 in the category of unconventional high-T_C superconductors, and its chemical uniqueness may help shed light on the high-T_C phenomena.

I. INTRODUCTION

Superconducting properties of high-T_C cuprates emerge from an intricate interplay between electronic, lattice, and spin degrees of freedom [1,2]. The cuprate crystal structure is generally derived from the perovskite-type structure, featuring a few universal themes. Structurally they all contain quasi-two-dimensional (2D) CuO_2 sheets. Their normal state electronic structure near the Fermi energy is dominated by a single band derived from Cu-d orbitals [1–6]. In sharp contrast to conventional superconductors based on electron-phonon coupling assisted Cooper pair formation, superconductivity in cuprates is believed to be driven largely by strong electronic interactions [6]. The quasi-2D nature of the crystal structure limits the electronic modes in the out-of-plane direction, resulting in reduced screening and an enhanced interaction that are essential to high-T_C superconductivity. Understanding obtained from the extensive studies of structural, electronic, and superconducting properties of cuprates has led to discoveries of new superconducting materials [6–8]. Insights into the interplay of geometric and electronic structures are key to the discovery of novel superconductors. Clearly, it is then attractive to assay materials that resemble cuprates, both structurally and electronically, for potential novel superconductivity.

Materials hosting divalent silver are extremely scarce in comparison with monovalent silver compounds. Silver difluoride (AgF_2) has been synthesized from $AgNO_3$, anhydrous hydrogen fluoride treated with K_2NiF_6 and elemental fluorine, with silver ion Ag(II) in a highly unusual divalent state despite the relatively large second ionization potential compared to the first one [9,10]. More interestingly, AgF_2 resembles the cuprates's parent phase La_2CuO_4 in its geometric, electronic, and magnetic structures. An AgF_2 sheet of the bulk crystal is structurally similar to a CuO_2 sheet, with a similar pattern of out-of-plane displaced anion atoms as shown in Fig. 1(a). The divalent Ag features a $4d^9$ valence shell, isovalent to cuprates. The antiferromagnetic ground state of charge neutral AgF_2 is a charge-transfer insulator, which again is a familiar scenario in cuprates.

It is then a natural and tempting question to ask whether AgF_2 could be metallized upon doping and become superconducting, such as the cuprates. Various theoretical attempts have been made to study the doping mechanism of carriers in AgF_2 [11–14]. It is therefore the purpose of this work to study whether an interaction can drive a superconducting transition in AgF_2, and what the ensuing pairing symmetry will be. We start with an investigation of the crystal and electronic structure of AgF_2 and its resemblance to the archetypal cuprate, orthorhombic La_2CuO_4 [6]. A comparison of the crystal and electronic structures obtained from first-principles calculations establishes a compelling structural and electronic resemblance between these compounds. A multiband Hubbard model is constructed from which the spin susceptibility of AgF_2 within the random-phase approximation reveals an antiferromagnetic instability in accordance with experiments. Employing the fluctuation-exchange approximation and solving the linearized Eliashberg equations, we obtain the superconducting pairing strength (λ) and symmetry. A phase diagram is obtained by calculating λ at various carrier doping levels and Hubbard U values. The strongest superconducting pairing is obtained at 5% electron doping for bulk AgF_2, with a dominating singlet d_{xz} symmetry. We find that the superconducting pairing strength is gradually noted to increase with decreasing interlayer coupling. We attribute this effect to the renormalization of electron-electron correlations with decreasing out-of-plane coupling.

*These authors contributed equally to this work.
†jfeng11@pku.edu.cn

II. METHODOLOGY

A. Density-functional theory calculations

Density-functional theory calculations have been performed using the projector-augmented wave method [15,16], implemented within the Vienna *ab initio* simulation package (VASP) [17]. The Perdew-Burke-Ernzerhof functional [18] is used for the exchange-correlation functional, and an additional electron-electron correlation is included statically by a $U = 8$ eV within the generalized gradient approximation (GGA+U) formalism [19]. The value of U on the Ag-d orbital is chosen to match the experimentally observed Ag magnetic moments of $0.7\mu_B$/Ag. The results are found to be well converged with a $6 \times 6 \times 8$ Γ-centered mesh of k points and a plane-wave cutoff of 800 eV. The total energy is calculated self-consistently until the energy difference between successive steps is below 10^{-5} eV. The experimental lattice parameters of orthorhombic AgF$_2$ with space group *Pbca* (No. 61) are $|\mathbf{a}| = 5.101$ Å, $|\mathbf{b}| = 5.568$ Å, and $|\mathbf{c}| = 5.831$ Å [20]. Considering the experimentally observed magnetic ground state, a full optimization of the lattice parameters has been performed. The changes in the **a** and **b** lattice constants were found to be less than 1% while the **c** vector was enhanced by ~1.7%. Since these values are very close to the experimental ones, the experimental structure is used for further study.

B. Random-phase approximation and fluctuation-exchange approximation

To investigate the effect of interaction on the magnetic order and potential superconductivity, we construct a multiband Hubbard model,

$$H = H_0 + H_U = \sum_{ijll'\sigma} t_{ij}^{ll'} c_{il\sigma}^\dagger c_{jl'\sigma} + U \sum_{il} n_{il\uparrow} n_{il\downarrow}, \quad (1)$$

where i, l, and σ are the lattice, orbital, and spin indices, respectively, and c and n are the fermion annihilation and number operators, respectively. The intraorbital Hubbard parameter U is determined by estimating the Néel temperature in a random-phase approximation (RPA), as described next.

The low-energy bands are described by a tight-binding Hamiltonian H_0, obtained by projecting the non-spin-polarized *ab initio* band structure using the maximally localized Wannier function approach [21], implemented within VASP. Mapping is done for the undoped case considering Ag-$d_{x^2-y^2}$ orbitals in the basis and the obtained hopping amplitudes are listed in Table I.

Within the RPA [22–26], the charge (χ^c) and spin (χ^s) susceptibilities are given by

$$\chi^c(q) = [1 + \chi^0(q)U^c]^{-1}\chi^0(q),$$
$$\chi^s(q) = [1 - \chi^0(q)U^s]^{-1}\chi^0(q), \quad (2)$$

where $q = (\mathbf{q}, \omega)$. U^c and U^s are the interaction matrices in the charge and spin channels, respectively, and are written as

$$(U^{c/s})_{l_3l_4}^{l_1l_2} = \begin{cases} U, & l_1 = l_2 = l_3 = l_4, \\ 0, & \text{otherwise}. \end{cases} \quad (3)$$

TABLE I. List of all hopping amplitudes larger than 5 meV in our Wannier function-based tight-binding model of bulk AgF$_2$. **R** and l/l' are the translation vector and orbital index, respectively. All other hoppings not listed here can be obtained by applying symmetry operations of *Pbca*, the space group of bulk AgF$_2$.

R	l	l'	t (meV)
$(0, 0, 0)$	1	2	-173.1
$(1, -1, 0)$	1	1	34.4
$(0, 1, 0)$	1	1	34.0
$(0, 1, -1)$	1	1	28.0
$(0, -1, 0)$	1	3	22.8
$(0, 0, -1)$	1	2	18.2
$(1, 0, -1)$	1	1	18.1
$(1, 1, 0)$	1	1	15.1
$(0, 1, 0)$	1	3	-11.4
$(0, 0, 0)$	1	4	7.8
$(1, 0, 1)$	1	1	7.1
$(0, 0, 0)$	1	3	-7.0
$(1, 0, 0)$	1	4	-6.1
$(1, -1, -1)$	1	1	-5.6
$(1, 0, 0)$	1	3	5.3
$(1, 0, 0)$	1	1	5.1

The bare susceptibility $\chi^0(q)$ is described as

$$(\chi^0)_{l_3l_4}^{l_1l_2}(\mathbf{q}, \omega) = -\frac{1}{N} \sum_{\mathbf{k},\mu\nu} \frac{f(\varepsilon_{\mu\mathbf{k}} - \varepsilon_F) - f(\varepsilon_{\nu\mathbf{k+q}} - \varepsilon_F)}{\omega + \varepsilon_{\mu\mathbf{k}} - \varepsilon_{\nu\mathbf{k+q}} + i0^+}$$
$$\times \left[a_\nu^{l_2}(\mathbf{k+q}) a_\nu^{l_3*}(\mathbf{k+q}) a_\mu^{l_4}(\mathbf{k}) a_\mu^{l_1*}(\mathbf{k}) \right], \quad (4)$$

where N is the number of $\mathbf{k}$ points and μ, ν are the band indices. $a_\mu^l(\mathbf{k})$ is the l component of the wave function of band μ at the $\mathbf{k}$ point and $\varepsilon_{\mu\mathbf{k}}$ are the corresponding eigenvalues, obtained from the diagonalization of H_0. $f(\varepsilon)$ is the Fermi-Dirac distribution and ε_F is the Fermi energy.

The scrutiny for potential superconductivity mediated by spin fluctuations is done by employing the fluctuation-exchange approximation (FLEX) [27,28] to describe the effective electron-electron interaction $\Gamma(q)$ given by

$$\Gamma(q) = \gamma U^s \chi^s(q) U^s - \frac{1}{2} U^c \chi^c(q) U^c + \frac{1}{2}(U^s + U^c), \quad (5)$$

with $\gamma = \frac{3}{2}$ for the singlet channel and $\gamma = -\frac{1}{2}$ for the triplet channel. The singlet vertex is symmetrized as

$$(\Gamma^s)_{l_3l_4}^{l_1l_2}(k, k') \leftarrow \frac{1}{2}\left[(\Gamma^s)_{l_3l_4}^{l_1l_2}(k, k') + (\Gamma^s)_{l_3l_2}^{l_1l_4}(k, -k')\right], \quad (6)$$

and the triplet vertex is antisymmetrized as

$$(\Gamma^t)_{l_3l_4}^{l_1l_2}(k, k') \leftarrow \frac{1}{2}\left[(\Gamma^t)_{l_3l_4}^{l_1l_2}(k, k') - (\Gamma^t)_{l_3l_2}^{l_1l_4}(k, -k')\right]. \quad (7)$$

Here, $\Gamma(k, k') = \Gamma(q)$ with $q = k - k'$.

An effective pairing between the electrons on the Fermi surface arising from spin and/or charge fluctuations can result in the formation of Cooper pairs. To describe the pairing instability of this type, the linearized Eliashberg equation will then be solved to obtain the order parameter and superconducting

transition temperature,

$$\lambda \phi_{l_1 l_3}(k) = -\frac{T}{N} \sum_q \sum_{l_2 l_4 l_5 l_6} \Gamma^{l_1 l_2}_{l_3 l_4}(q) \phi_{l_5 l_6}$$

$$\times (k-q) G_{l_2 l_5}(k-q) G_{l_4 l_6}(q-k). \qquad (8)$$

Here, λ is the eigenvalue indicating the pairing strength. The eigenvector $\phi_{l_1 l_2}(k)$ is the order parameter written in terms of the orbital indices l_1 and l_2. $G_{l_1 l_2}(k)$ is the Matsubara Green's function. The largest eigenvalue $\lambda_{\max}$ becomes unity at superconducting T_C and can be used to gauge the relative pairing strength near the T_C.

In the weak-coupling regime, the pairing vertex is approximated to be frequency independent, i.e., $\Gamma(q) = \Gamma(\mathbf{q}, \omega = 0)$. After summing over the Matsubara frequencies, we obtain the following equation in the band basis,

$$\lambda \phi_{mn}(\mathbf{k}) = -\frac{1}{N} \sum_{\mathbf{k}'} \sum_{\mu\nu} \Gamma^{mn}_{\mu\nu}(\mathbf{k}, \mathbf{k}') F_{\mu\nu}(\mathbf{k}') \phi_{\mu\nu}(\mathbf{k}'), \qquad (9)$$

where

$$F_{\mu\nu}(\mathbf{k}) = -\frac{f(\varepsilon_{\mu\mathbf{k}} - \varepsilon_F) + f(\varepsilon_{\nu-\mathbf{k}} - \varepsilon_F) - 1}{\varepsilon_{\mu\mathbf{k}} + \varepsilon_{\nu-\mathbf{k}} - 2\varepsilon_F}. \qquad (10)$$

The transformation between the orbital basis and band basis for the order parameter is

$$\phi_{\mu\nu}(\mathbf{k}) = \sum_{l_1 l_2} \phi_{l_1 l_2}(\mathbf{k}) a^{l_1*}_\mu(\mathbf{k}) a^{l_2*}_\nu(-\mathbf{k}), \qquad (11)$$

and for the vertex,

$$(\Gamma^\eta)^{mn}_{\mu\nu}(\mathbf{k}, \mathbf{k}') = \sum_{l_1 l_2 l_3 l_4} a^{l_1*}_m(\mathbf{k}) a^{l_3*}_n(-\mathbf{k}) (\Gamma^\eta)^{l_1 l_2}_{l_3 l_4}$$

$$\times (\mathbf{k} - \mathbf{k}') a^{l_2}_\mu(\mathbf{k}') a^{l_4}_\nu(-\mathbf{k}'). \qquad (12)$$

Since $\phi_{\mu\nu}(\mathbf{k})$ is not gauge invariant because of the eigenvector $a^l_\mu(\mathbf{k})$ involved in Eq. (11), the trace of $\phi_{\mu\nu}(\mathbf{k})$, $\phi(\mathbf{k}) = \sum_\mu \phi_{\mu\mu}(\mathbf{k}) \delta(\varepsilon_{\mu\mathbf{k}} - \varepsilon_F)$, taken on the Fermi surface is used to describe the nature of the order parameter, which is gauge invariant under the following condition,

$$a^l_\mu(-\mathbf{k}) = a^l_\mu(\mathbf{k})^*, \qquad (13)$$

for the nonmagnetic state [29]. An energy cutoff of 5 meV is considered for the evaluation of the δ function in our calculations.

III. RESULTS

A. Crystal and electronic structure

The structure of AgF_2 can be viewed as a stack of Ag-F square-planar networks resembling the cuprate planes in La_2CuO_4 [6] as shown in Fig. 1(a). Similar to the low-temperature polymorph of La_2CuO_4 [6], AgF_2 has an orthorhombic crystal structure with each Ag(II) in a distorted octahedral crystal field of six nearest-neighbor F^- ions [20,30]. However, unlike in a perfect octahedral coordination, the out-of-plane Ag-F bonds are elongated by 24% relative to the in-plane ones as shown by the blue dashed lines on one of the Ag(II) in Fig. 1(a), leaving Ag(II) 4-coordination in a AgF_2 unit. This again resembles La_2CuO_4 in which there
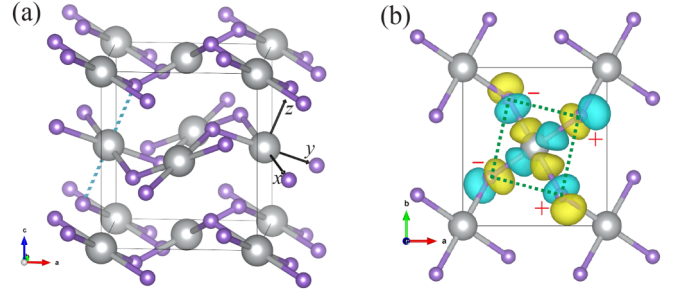
FIG. 1. (a) AgF_2 crystal structure. Purple and gray balls are F and Ag, respectively. Blue dashed lines through one of the Ag(II) indicate out-of-plane Ag-F bonds in a AgF_6 octahedron. The black arrows labeled x, y, z indicate the local coordinates used to describe the d orbitals on Ag. In (b), the green dash-lined box highlights a AgF_4 unit. $+/-$ indicate out-of-plane displacements of fluoride ions. The $d_{x^2-y^2}$ Wannier orbital on the central Ag is shown.

is a 27% elongation of the out-of-plane Cu-O bonds. These four F^--coordinated Ag(II) form the AgF_4 unit within the square-planar network, as indicated by the green dash-lined box in Fig. 1(b). A significant deviation of the AgF_2 structure from La_2CuO_4 comes from the tilting of this AgF_4 unit by a large angle $\sim 25°$, and hence the plane is puckered as shown in Fig. 1. This tilt of CuO_4 in La_2CuO_4 is much gentler ($\sim 5°$). The TM-anion-TM (TM = Ag or Cu) angles in the square-planar structure are $\sim 130°$ for AgF_2, which is $\sim 173°$ in La_2CuO_4. This distortion from the ideal $180°$ angle is expected to manifest itself in the superexchange interaction, and therefore the temperature of magnetic ordering. Indeed, the Néel temperature (T_N) is 300 K for La_2CuO_4 and 163 K for AgF_2 [31,32]. Given the striking similarities in the structural and magnetic properties of AgF_2 with those of La_2CuO_4 and the subtle difference, an investigation of its electronic properties in the context of superconductivity is warranted.

As discussed earlier, a single $d_{x^2-y^2}$ orbital for AgF_2 shown in Fig. 1(b) dominating the low-energy space near the Fermi level is one of the most prominent characteristic features similar to the cuprates. This is schematically shown in Fig. 2(a) where partially filled $d_{x^2-y^2}$, shown in red, contributes at the Fermi level. In the octahedral crystal field, the d orbitals are split into a triply degenerate t_{2g} set and a doubly degenerate e_g set. The deviation from perfect octahedral symmetry described earlier lifts the degeneracy of e_g orbitals with d_{z^2} being lower in energy than the in-plane $d_{x^2-y^2}$. The occupied anion $2p$ orbitals are situated deep below the Fermi level. The calculated orbital-projected band structure in spin-up and spin-down channels within the GGA+U formalism for the antiferromagnetic arrangement of AgF_2 is shown in Fig. 2(b). The valence band near the Fermi level has a dominant contribution from $d_{x^2-y^2}$ orbitals which are occupied in the majority spin channel at Ag sites following the magnetic ground state shown in Fig. 3(d).

The band structure of nonmagnetic AgF_2, calculated within GGA formalism without U, shown in Fig. 3(a) exhibits features akin to cuprates. The low-energy excitations are dominated by the half-filled $d_{x^2-y^2}$ on Ag, and are well separated from all other bands. Thus when constructing a tight-binding model, it is justified to include simply one $d_{x^2-y^2}$-like Wannier
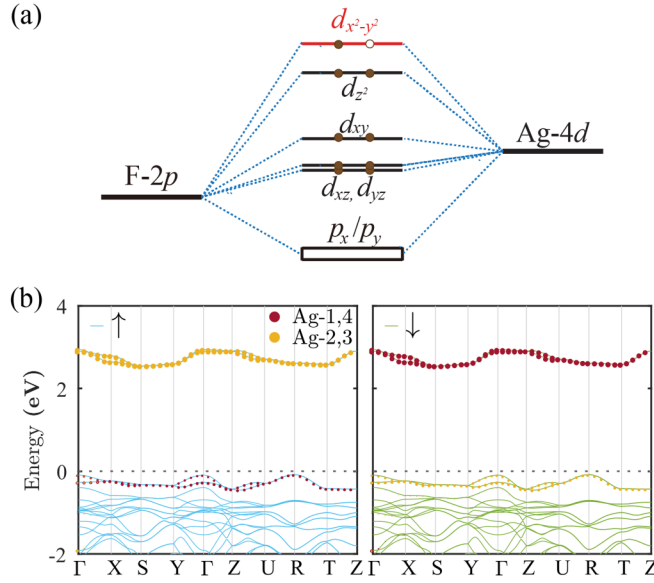
FIG. 2. (a) Schematic energy level diagram of Ag(II) in the crystal field of F atoms. (b) The band structure of antiferromagnetic AgF_2 in spin-up and spin-down channels. Contributions of $d_{x^2-y^2}$ orbital from different Ag sites (1–4) are color coded with solid dots. The indices of Ag sites can be found in Fig. 3(d). The Fermi energy is set to 0 and indicated by the gray dashed line.

orbital per Ag. The resultant band structure of the tight-binding model is also shown in Fig. 3(a), where the four $d_{x^2-y^2}$ bands (four Ag per unit cell) fit the first-principles bands well. Once the Coulomb interaction is included, AgF_2 becomes a charge-transfer antiferromagnetic insulator similar to the cuprates in a scenario discussed also by Jakub *et al.* [9].
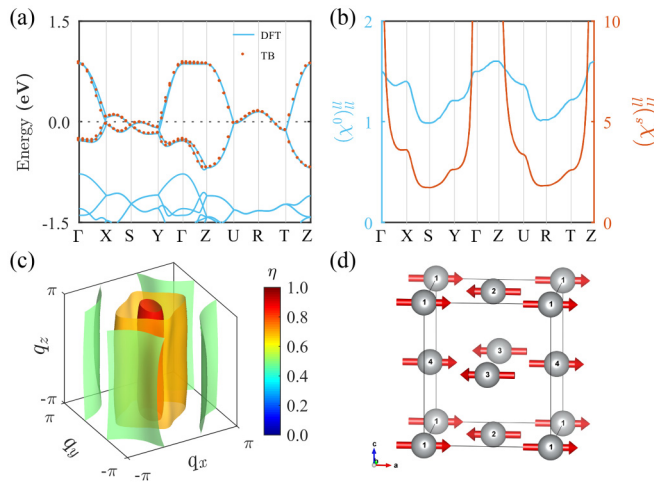
FIG. 3. (a) The band structure of nonmagnetic AgF_2 from first-principles calculation (DFT) and the Wannier interpolation-based tight-binding model (TB) shown near the Fermi energy. (b) Diagonal elements of the bare susceptibility $(\chi^0)_{ll}^{ll}(\boldsymbol{q}, 0)$ and the spin susceptibility $(\chi^s)_{ll}^{ll}(\boldsymbol{q}, 0)$ along the high-symmetry path, where $l = 1$–4 is the orbital index. The four curves coincide. (c) $\eta(\boldsymbol{q})$ for undoped bulk AgF_2 with isovalue 0.5 (cyan), 0.7 (yellow), and 0.9 (red). Here, $U = 0.44$ eV and $T = 14$ meV. (d) Magnetic structure of AgF_2 obtained from RPA. Red arrows represent the magnetic moment on Ag atoms.

B. Spin susceptibility

The onset of spin instability is detected by the condition $|1 - \chi^0(\boldsymbol{q}, 0)U^s| = 0$, which occurs when the maximum eigenvalue of $\chi^0(\boldsymbol{q}, 0)U^s$ [denoted by $\eta(\boldsymbol{q})$] becomes unity at any $\boldsymbol{q}$. The ensuing divergence of χ^s leads to a magnetic phase transition. The vector $\boldsymbol{q}^*$ and temperature T_N at which $\eta(\boldsymbol{q}^*) = 1$ are the Néel temperature and propagation vector of the spin pattern, respectively. The spin pattern corresponding to a $\boldsymbol{q}^*$ is determined by diagonal elements of the eigenvector $\xi(\boldsymbol{q}^*)$ corresponding to $\eta(\boldsymbol{q}^*)$. We use a mesh of $48 \times 48 \times 48$ for Brillouin zone sampling in all our calculations on the Hubbard model.

Figure 3(b) shows the diagonal elements of the bare susceptibility $(\chi^0)_{ll}^{ll}(\boldsymbol{q}, 0)$ and the spin susceptibility $(\chi^s)_{ll}^{ll}(\boldsymbol{q}, 0)$ along the high-symmetry paths in the reciprocal space. The smooth variation of these susceptibilities in the plot highlights the good convergence of our results. To determine the Hubbard U, we tune the value of U to match the experimental Néel temperature (~ 163 K) of AgF_2 with the RPA estimated transition temperature. This leads to $U = 0.44$ eV, which will be used in the following calculations on bulk AgF_2. We note that this U value is lower than the screened Hubbard $U = 2.7$ eV from a constrained RPA [33–35] implemented within VASP [17]. But since the latter contains double counting and does not reproduce the experimental T_N, we use the former value for subsequent FLEX calculations.

Isosurfaces of $\eta(\boldsymbol{q})$ drawn in Fig. 3(c) for undoped bulk AgF_2 at $T = 14$ meV (~ 163 K) show a strong anisotropy corresponding to strong intralayer and a weak interlayer magnetic exchange interactions. Henceforth, we focus on the $q_z = 0$ plane in the current analysis. The maximum value of $\eta(\boldsymbol{q})$ is found to lie along the q_z axis. Thus, for a weak interlayer coupling when restricted only in the q_x-q_y plane, the maximum value of the spin susceptibility is attained at $\boldsymbol{q} = 0$. The computed eigenvectors $\xi_{ll}(\boldsymbol{q} = 0)$ yield an antiferromagnetic order shown in Fig. 3(d), consistent with the experimentally established Néel state in AgF_2 [32].

C. Interaction-mediated superconductivity

When doped with a carrier concentration that readily suppresses the magnetism, a cuprate goes metallic, exhibiting various kinds of instabilities such as charge and spin fluctuations at low temperatures due to Fermi-surface reconstruction. The Hubbard models have been used extensively to explain the superconductivity in doped cuprates [7]. Keeping the striking resemblance of AgF_2 with cuprates, a similar approach of metallization by carrier doping applies in AgF_2 as well. Thus, having a model capable of describing the magnetic instability and order of AgF_2, we go on to search for potential superconductivity mediated by spin fluctuation employing the fluctuation-exchange approximation (FLEX) as discussed in the methodology section.

Equation (9) is solved for various doping levels and U values at $T = 30$ meV. Figure 4(a) shows the contour plot for λ_{max} in the $U - \delta n$ parameter space. As observed in Fig. 4(a), the superconducting pairing strength increases with increasing U at a given doping, underlining the importance of electronic correlations for potential superconductivity in this compound. The symmetry of pairing can be identified by
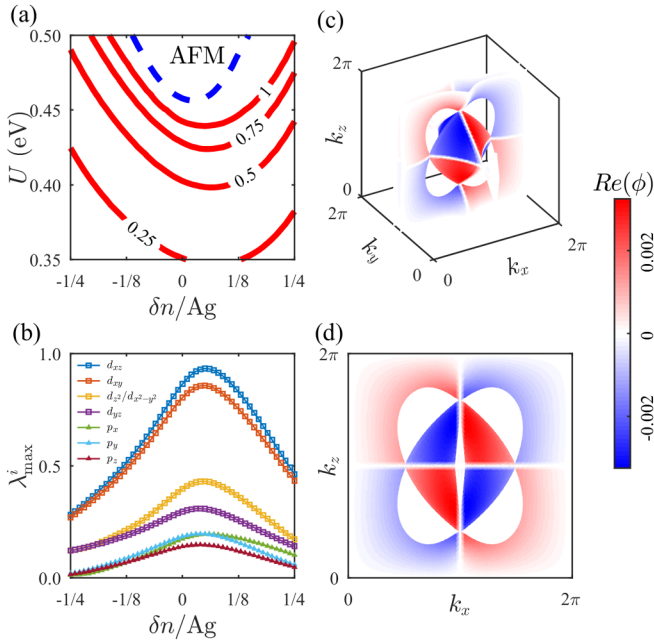
FIG. 4. (a) Contour plot of λ_{max} of the linearized Eliashberg equation at $T = 30$ meV. The blue dashed line corresponds to $\eta(\boldsymbol{q})$ reaching unity at any $\boldsymbol{q}$. (b) Doping dependence of λ^i_{max} for several pairing symmetries of bulk AgF_2 at $U = 0.44$ eV and $T = 30$ meV. The squares and triangles represent the singlet and triplet channels, respectively. (c) Three-dimensional and (d) projection on the k_x-k_z plane, of the order parameter $\phi(\boldsymbol{k})$ at the Fermi surface of one of the AgF_2 layers with $\delta n/Ag = 0.05$ for bulk AgF_2.

assigning each solved $\phi_{mn}(\boldsymbol{k})$ to an irreducible representation of the D_{2h} point group [36], the symmetry group of the bulk AgF_2. Corresponding to each irreducible representation i, the largest eigenvalue is denoted by λ^i_{max}. Figure 4(b) shows the doping dependence of λ^i_{max} for various pairing symmetries at $U = 0.44$ eV. One can find that the singlet d-wave pairings have a significantly higher strength than triplet p-wave pairings and the leading pairing symmetry is a singlet d_{xz}-type wave throughout the $U - \delta n$ parameter space shown in Fig. 4(a). Moreover, the hole doping readily decreases λ, while the electron doping tends to increase λ at first, reaching a peak value at an optimal doping of 5% beyond which further doping tends to reduce λ.

To describes the nature of the order parameter on the Fermi surface, we plot the real part of the order parameter $\phi(\boldsymbol{k})$ corresponding to λ_{max} for one of the AgF_2 layers with $U = 0.44$ eV and an optimal doping of 5%. This is shown in Fig. 4(c) in the three-dimensional Brillouin zone, and Fig. 4(d) shows a projection onto the k_x-k_z plane. One encounters nodes crossing the $k_x = \pi$ or $k_z = \pi$ planes indicating a d_{xz}-wave pairing. Hence, it can be concluded that the bulk AgF_2 crystal becomes unstable to a d-wave pairing induced by a spin fluctuation.

D. Interlayer coupling

As discussed in the beginning, the quasi-2D nature of the crystal structure of cuprates is one of the factors favoring its high T_C [37,38]. In the case of AgF_2, although Ag-F layers

resemble copper oxide sheets, the separation of these planes is 2.91 Å, much smaller than what is observed for La_2CuO_4 (6.6 Å) as well as other cuprates. Consequently, the effect of interlayer coupling on the superconducting properties of AgF_2 clearly warrants further study. In other words, AgF_2 provides a good platform to investigate the role of the quasi-2D nature of the crystal structure in superconducting properties. Additionally, monolayer or few-layer samples are more prone to doping by techniques such as field or electrolytic gating [39], which is a clear experimental advantage.

To study the effect of interlayer coupling on the superconducting properties of AgF_2, we interpolate between the bulk and monolayer limits as follows,

$$H_0 = H^{intra} + \alpha H^{inter}. \tag{14}$$

Here, H^{intra} is a tight-binding model within a single layer of AgF_2, while H^{inter} is the interlayer hopping term, which is scaled by $\alpha \in [0, 1]$. Bulk AgF_2 can be obtained with $\alpha = 1$, and $\alpha = 0$ corresponds to a single layer of AgF_2. In the case of the monolayer, the reduced screening leads to a divergent pairing vertex if the bulk U value is used. This is an artifact of the linearized Eliashberg theory that occurs when the calculations are performed at temperatures much lower than the T_C, and one cannot get any sensible information about the superconducting behavior in this case. However, a qualitative estimation of the pairing symmetry can be obtained by slightly reducing the U value which helps in achieving the numerical convergence when moving away from the bulk to monolayer limit. Hence, we use $U = 0.37$ eV, the closest usable value to the bulk one, in the following calculations.

In Fig. 5(a), $\lambda^{d_{xy}}_{max}$ and $\lambda^{d_{xz}}_{max}$ are shown as functions of doping concentrations for different interlayer coupling strengths α. It can be seen that the interlayer coupling tends to suppress the superconducting pairing in both hole and electron doping because a stronger interlayer coupling amounts to weaker electronic correlations as discussed earlier. Evidently the quasi-2D nature of the crystal structure is one of the crucial factors in favor of high-T_C superconductivity, which again confirms the resemblance to cuprates. The optimal electron doping concentration remains unchanged as of bulk AgF_2, which indicates that the Fermi-surface nesting responsible for the divergence of spin susceptibility mainly occurs within a single layer without any significant interlayer contribution. In the absence of interlayer coupling, the separated monolayers have the same leading pairing symmetry of d_{xy} type. These two degenerate d_{xy} waves then split into d_{xz} and d_{xy} immediately after the interlayer coupling was switched on. The difference in pairing strength between the leading d_{xz} wave and competing d_{xy} was also found to increase with an increase of α.

For single-layer AgF_2, the symmetry reduces to the C_{2h} point group [36] from the D_{2h} of bulk AgF_2. Performing a similar analysis to that for the bulk, we show the doping dependence of λ^i_{max} for several pairing symmetries for a single layer in Fig. 5(b). As seen previously in Fig. 5(a), the leading pairing symmetry is d_{xy} followed by a $d_{x^2-y^2}$ wave. The real part of the $\phi(\boldsymbol{k})$ corresponding to the λ_{max} at the optimal doping concentration is shown in Fig. 5(c), which clearly reveals d_{xy} pairing symmetry in the monolayer limit.
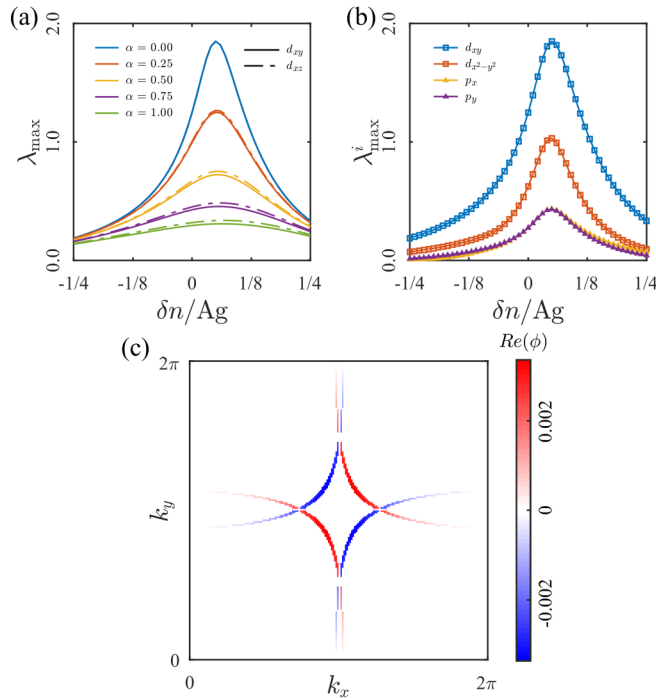
FIG. 5. (a) Doping dependence of $\lambda_{max}^{d_{xy}}$ and $\lambda_{max}^{d_{xz}}$ for different interlayer couplings α at $U = 0.37$ eV and $T = 30$ meV. (b) Doping dependence of λ_{max}^i of various pairing symmetries in single-layer AgF$_2$. (c) Plot of order parameter $\phi(\boldsymbol{k})$ in the k_x-k_y plane at the Fermi surface in single-layer AgF$_2$ with $\delta n/$Ag $= 0.05$.

IV. CONCLUSION AND OUTLOOK

Our calculations indicate AgF$_2$ not only is chemically exotic, but also harbors unconventional superconductivity in a way very similar to high-T_C cuprates. Our multiband Hubbard model reveals a magnetic instability in accordance with the experimentally obtained magnetic ground state. In the fluctuation-exchange approximation, we find a superconducting ground state with a singlet d-wave pairing for the bulk AgF$_2$ at an optimal electron doping of 5%. By varying the strength of the interlayer interaction, we show that the superconducting pairing strength increases with decreasing interlayer coupling, highlighting the crucial role played by quasi-2D crystal structures on the superconducting properties of such materials.

Drawing hints from cuprates, the metallization of bulk AgF$_2$ can be achieved by synthesizing it with a modified composition as is done in the case of La$_{2-x}$Ba$_x$CuO$_4$/La$_{2-x}$Sr$_x$CuO$_4$ [1,40], leading to the doping of extra charge carriers in the transition metal–anion plane. Another route to metallization is electric gating [41]. A monolayer of AgF$_2$ may be realized by epitaxial growth [42], whose metallization can be achieved during the deposition process. The idea of liquid-gating-induced superconductivity in thin films [43] can also be applied to monolayer AgF$_2$. Interestingly, a monolayer sample on a substrate [42] or in a quantum well may offer unique opportunities for tuning the dielectric environment of the sample, allowing for investigations of the effects of varying interactions on, especially, the proposed superconductivity.

[1] J. G. Bednorz and K. A. Müller, Z. Phys. B: Condens. Matter **64**, 189 (1986).

[2] J. G. Bednorz, M. Takashige, and K. A. Müller, Europhys. Lett. **3**, 379 (1987).

[3] J. G. Bednorz and K. A. Müller, Rev. Mod. Phys. **60**, 585 (1988).

[4] E. Dagotto, Rev. Mod. Phys. **66**, 763 (1994).

[5] M. A. Kastner, R. J. Birgeneau, G. Shirane, and Y. Endoh, Rev. Mod. Phys. **70**, 897 (1998).

[6] D. J. Scalapino, Rev. Mod. Phys. **84**, 1383 (2012).

[7] G. R. Stewart, Rev. Mod. Phys. **83**, 1589 (2011).

[8] Y. Cao, V. Fatemi, S. Fang, K. Watanabe, T. Taniguchi, E. Kaxiras, and P. Jarillo-Herrero, Nature (London) **556**, 43 (2018).

[9] J. Gawraczyński, D. Kurzydłowski, R. A. Ewings, S. Bandaru, W. Gadomski, Z. Mazej, G. Ruani, I. Bergenti, T. Jaroń, A. Ozarowski, S. Hill, P. J. Leszczyński, K. Tokár, M. Derzsi, P. Barone, K. Wohlfeld, J. Lorenzana, and W. Grochala, Proc. Natl. Acad. Sci. USA **116**, 1495 (2019).

[10] C. Miller and A. S. Botana, Phys. Rev. B **101**, 195116 (2020).

[11] N. Bachar, K. Koteras, J. Gawraczynski, W. Trzcinski, J. Paszula, R. Piombo, P. Barone, Z. Mazej, G. Ghiringhelli, A. Nag, K.-J. Zhou, J. Lorenzana, D. van der Marel, and W. Grochala, arXiv:2105.08862.

[12] M. Derzsi, K. Tokár, P. Piekarz, and W. Grochala, Phys. Rev. B **105**, L081113 (2022).

[13] S. Bandaru, M. Derzsi, A. Grzelak, J. Lorenzana, and W. Grochala, Phys. Rev. Materials **5**, 064801 (2021).

[14] Kamil Tokár, M. Derzsi, and W. Grochala, Comput. Mater. Sci. **188**, 110250 (2021).

[15] G. Kresse and D. Joubert, Phys. Rev. B **59**, 1758 (1999).

[16] P. E. Blöchl, Phys. Rev. B **50**, 17953 (1994).

[17] G. Kresse and J. Furthmüller, Phys. Rev. B **54**, 11169 (1996).

[18] J. P. Perdew, K. Burke, and M. Ernzerhof, Phys. Rev. Lett. **77**, 3865 (1996).

[19] S. L. Dudarev, G. A. Botton, S. Y. Savrasov, C. J. Humphreys, and A. P. Sutton, Phys. Rev. B **57**, 1505 (1998).

[20] P. Charpin, P. Plurien, and P. Meriel, Bull. Soc. Fr. Mineral. Cristallogr. **93**, 7 (1970).

[21] A. A. Mostofi, J. R. Yates, Y.-S. Lee, I. Souza, D. Vanderbilt, and N. Marzari, Comput. Phys. Commun. **178**, 685 (2008).

[22] S. Graser, T. A. Maier, P. J. Hirschfeld, and D. J. Scalapino, New J. Phys. **11**, 025016 (2009).

[23] T. A. Maier, S. Graser, P. J. Hirschfeld, and D. J. Scalapino, Phys. Rev. B **83**, 100515(R) (2011).

[24] K. Kuroki, S. Onari, R. Arita, H. Usui, Y. Tanaka, H. Kontani, and H. Aoki, Phys. Rev. Lett. **101**, 087004 (2008).

[25] X. Wu, F. Yang, C. Le, H. Fan, and J. Hu, Phys. Rev. B **92**, 104511 (2015).

[26] K. Kuroki, H. Usui, S. Onari, R. Arita, and H. Aoki, Phys. Rev. B **79**, 224511 (2009).

[27] N. E. Bickers, D. J. Scalapino, and S. R. White, Phys. Rev. Lett. **62**, 961 (1989).

[28] T. Takimoto, T. Hotta, and K. Ueda, Phys. Rev. B **69**, 104504 (2004).

[29] A. F. Kemper, T. A. Maier, S. Graser, H.-P. Cheng, P. J. Hirschfeld, and D. J. Scalapino, New J. Phys. **12**, 073030 (2010).

[30] P. Fischer, D. Schwarzenbach, and H. Rietveld, J. Phys. Chem. Solids **32**, 543 (1971).

[31] N. P. Armitage, P. Fournier, and R. L. Greene, Rev. Mod. Phys. **82**, 2421 (2010).

[32] P. Fischer, G. Roult, and D. Schwarzenbach, J. Phys. Chem. Solids **32**, 1641 (1971).

[33] F. Aryasetiawan, M. Imada, A. Georges, G. Kotliar, S. Biermann, and A. I. Lichtenstein, Phys. Rev. B **70**, 195104 (2004).

[34] F. Aryasetiawan, K. Karlsson, O. Jepsen, and U. Schönberger, Phys. Rev. B **74**, 125106 (2006).

[35] Y. Nomura, M. Kaltak, K. Nakamura, C. Taranto, S. Sakai, A. Toschi, R. Arita, K. Held, G. Kresse, and M. Imada, Phys. Rev. B **86**, 085117 (2012).

[36] M. I. Aroyo, A. Kirov, C. Capillas, J. M. Perez-Mato, and H. Wondratschek, Acta Crystallogr., Sect. A **62**, 115 (2006).

[37] D. Jiang, T. Hu, L. You, Q. Li, A. Li, H. Wang, G. Mu, Z. Chen, H. Zhang, G. Yu, J. Zhu, Q. Sun, C. Lin, H. Xiao, X. Xie, and M. Jiang, Nat. Commun. **5**, 5708 (2014).

[38] Y. Yu, L. Ma, P. Cai, R. Zhong, C. Ye, J. Shen, G. D. Gu, X. H. Chen, and Y. Zhang, Nature (London) **575**, 156 (2019).

[39] J. T. Ye, Y. J. Zhang, R. Akashi, M. S. Bahramy, R. Arita, and Y. Iwasa, Science **338**, 1193 (2012).

[40] A. T. Bollinger, G. Dubuis, J. Yoon, D. Pavuna, J. Misewich, and I. Božović, Nature (London) **472**, 458 (2011).

[41] A. Goldman, Annu. Rev. Mater. Res. **44**, 45 (2014).

[42] A. Grzelak, H. Su, X. Yang, D. Kurzydłowski, J. Lorenzana, and W. Grochala, Phys. Rev. Materials **4**, 084405 (2020).

[43] J. T. Ye, S. Inoue, K. Kobayashi, Y. Kasahara, H. T. Yuan, H. Shimotani, and Y. Iwasa, Nat. Mater. **9**, 125 (2010).